

Ion temperature gradient turbulence close to the finite heat flux threshold

Cite as: Phys. Plasmas **24**, 102317 (2017); <https://doi.org/10.1063/1.4986035>

Submitted: 01 June 2017 • Accepted: 04 October 2017 • Published Online: 23 October 2017

 A. Weikl, A. G. Peeters, F. Rath, et al.



[View Online](#)



[Export Citation](#)



[CrossMark](#)

ARTICLES YOU MAY BE INTERESTED IN

Theory and simulation of rotational shear stabilization of turbulence

Physics of Plasmas **5**, 1784 (1998); <https://doi.org/10.1063/1.872847>

Comparisons and physics basis of tokamak transport models and turbulence simulations

Physics of Plasmas **7**, 969 (2000); <https://doi.org/10.1063/1.873896>

Gradient-driven flux-tube simulations of ion temperature gradient turbulence close to the non-linear threshold

Physics of Plasmas **23**, 082517 (2016); <https://doi.org/10.1063/1.4961231>

[Submit Today!](#)

Physics of Plasmas

**Special Topic: Plasma Physics
of the Sun in Honor of Eugene Parker**



Ion temperature gradient turbulence close to the finite heat flux threshold

A. Weikl,¹ A. G. Peeters,¹ F. Rath,¹ S. R. Grosshauser,¹ R. Buchholz,¹ W. A. Hornsby,²
F. Seiferling,¹ and D. Strintzi¹

¹Physics Department, University of Bayreuth, Universitätsstrasse 30 Bayreuth, Germany

²Max Planck Institut für Plasmaphysik, Boltzmannstrasse 2 85748 Garching, Germany

(Received 1 June 2017; accepted 4 October 2017; published online 23 October 2017)

The dependence of the heat flux on the temperature gradient length in collisionless ion temperature gradient turbulence has recently been revisited. It has been found that the heat flux is discontinuous at a finite heat flux threshold larger than the (Dimits) interpolated threshold. In this paper, the influence of collisions on the heat flux close to the threshold is investigated. It is found that up to relatively high collision frequencies, relevant to the modern day experiments, a discontinuous behaviour of the heat flux as a function of the gradient length persists. Collisions, however, do lead to a reduction in the gradient length at which the discontinuity is observed. Below the finite heat flux threshold, a state of low turbulence with a vanishing small heat flux persists, which can drive the zonal flow against the collisional dissipation. This state is characterised by the fully developed staircases in the radial ExB shearing profile. Increasing the collision frequency at a fixed gradient length leads to the loss of the fully developed staircase structure with the ExB shearing profile having the form of a sawtooth that allows for avalanche formation and a finite heat flux. At very high collision frequencies or gradient lengths well above the threshold the staircase structure is lost. The simulations indicate that the long wave length zonal flow saturates through a mechanism that directly involves the turbulence intensity. *Published by AIP Publishing.*

<https://doi.org/10.1063/1.4986035>

I. INTRODUCTION

In tokamaks, the turbulence generated by the ion temperature gradient (ITG) instability is regulated by the so-called zonal flows.¹ These poloidal flows are nonlinearly driven by the turbulence through the Reynolds stress and, in turn, reduce the turbulence through shear decorrelation.² The influence of the zonal flows is most prominent close to the threshold for turbulence generation, given by a specific temperature gradient length ($R/L_T \equiv -R\nabla T/T$). In a landmark paper,³ it was shown that this threshold is not determined by the linear stability of the ITG, but rather is nonlinearly up-shifted. For gradient lengths (R/L_T) in between the threshold for linear stability $R/L_{T,\text{lin}}$ and the so-called Dimits threshold $R/L_{T,\text{Dim}}$, the ITG is linearly unstable, but as the turbulence develops, it drives zonal flows that are sufficiently strong to suppress the turbulence, resulting in a state with a vanishing heat flux. The results of Ref. 3 were obtained in the collisionless case. Indeed, the collisional case is qualitatively different due to the collisional damping of the zonal flow. The heat flux below the Dimits threshold for the collisional case has been discussed in Ref. 4. It was found that for the collisional case also the zonal flow spins up and suppresses the turbulence below the Dimits threshold, but due to the collisional damping of the zonal flows the lifetime of the phase with vanishing heat flux is limited and the turbulence reappears again. This leads to an oscillatory behaviour in the heat flux, and a rise of the time averaged heat flux with collisionality.⁴

It has recently been shown^{5,6} that the picture given above is incomplete, at least for the collisionless case. The nonlinear threshold for turbulence generation is not given by the Dimits threshold, i.e., the threshold obtained by interpolating the

turbulent heat flux to zero. Rather, the threshold is given by the so-called finite heat flux threshold ($R/L_{T,\text{fh}}$), which is significantly up-shifted compared with the Dimits threshold. At the finite heat flux threshold, the heat flux does not change continuously, but rather shows a jump from a state where the turbulence is suppressed, and the heat flux vanishes to a state where a finite heat flux is present. The latter heat flux can be larger than the heat fluxes obtained under relevant experimental conditions and suggests that the experimental heat flux calculations must, at least in some cases, be obtained from the flux rather than the gradient driven simulations.⁵ The jump in the heat flux is shown to be related to the formation of staircases,⁶ which were first observed in fully developed turbulent simulations in Refs. 7–9. In the state where the turbulence is not suppressed, the finite heat flux is induced by avalanches.^{8,10} The simulations in Ref. 6, also show that sufficiently small dissipation is necessary to observe the finite heat flux threshold, and that in the region $R/L_{T,\text{Dim}} < R/L_T < R/L_{T,\text{fh}}$ the turbulent system takes a considerable amount of time to settle in the vanishing heat flux state, particularly close to the finite heat flux threshold. This raises the question whether the observation of the finite heat flux threshold is only of mere academic interest. Does a significant change in the behaviour compared to the results presented in Refs. 5 and 6 occur for experimentally relevant collision frequencies and how does this relate to previous understandings?^{1,4} It is this question that this paper will address.

This paper is structured as follows: Section II presents an analysis of the zonal flow damping by collisions. In Sec. III, the influence of the collision frequency on the turbulence and the finite heat flux threshold is examined. The corresponding

behaviour of the (radially averaged) shear intensity is shown in Sec. IV. In Sec. V, the interpretation of the correlation between the heat flux and the staircases is explained. Section VI gives the concluding discussion.

II. COLLISIONAL DAMPING OF ZONAL FLOWS

Before the influence of collisions on the finite heat flux threshold is examined, the collisional damping of the zonal flows is investigated in more detail. To this extent, the linear simulations with an initial radial charge separation, equivalent to the (undamped) residual zonal flow “Rosenbluth-Hinton”-test,^{11,12} are carried out with GKW.¹³ The collisions are included in this test, and the time evolution of the electrostatic potential ϕ connected with the zonal flow is examined. The potential consists of a decaying oscillation of a geodesic acoustic mode (GAM) and a slower decay of the residual potential. The latter contribution to the potential is thought to be responsible for the turbulence suppression, and its decay is related to the collisional damping of the zonal flow. The collisional damping rate of the residue is measured and compared with an analytic model.¹⁴

In the Rosenbluth-Hinton test, care has to be taken to mitigate the influence of the so-called recurrence-problem,^{15,16} which is caused by the phase-space-filamentation that cannot be resolved on the discrete velocity-space grid, leading to a non-physical recurrence of the GAM-oscillation. The duration for which a simulation is physically correct is determined by its grid-resolution, and the long simulation times are therefore connected with high computational resource demands. As phase-space-filamentation is suppressed by dissipation, this problem appears mainly in the low collisionality-regime. But to ensure compatibility, the same resolution is used for all collision frequencies in this paper. To limit computational costs, measures are taken to decrease the required length of the simulations. The parameters are chosen to feature a relatively quick decay of the GAM, allowing for a longer unobstructed view of the potential. A geometry with circular concentric flux-surfaces is used, with a safety factor $q = 1.3$, the magnetic shear $\hat{s} = 0.1$, and an inverse aspect ratio $\varepsilon = 0.15$. The following grid sizes are used: $N_s = 128$, $N_\mu = 96$, and $N_{v\parallel} = 512$, where N_s is the number of grid points along the field line, N_μ is the magnetic moment, and $N_{v\parallel}$ is the parallel (to the magnetic field) velocity direction. A spectral representation is used for the directions perpendicular to the field, and only one radial wave vector with $k_r \rho \ll 1$ is retained. The relatively high resolution in $v\parallel$ and μ is used to mitigate the recurrence problem. Furthermore, to prevent vitiation of the collision’s influence, no numerical dissipation is applied in all directions. All simulations mentioned in this paper are performed with GKW, neglect plasma rotation, and use the electrostatic limit with the adiabatic electron response. The ion-ion collisions are modelled with a pitch-angle scattering collision operator. The corresponding normalized collision frequency is defined as

$$\nu_{ii} = \frac{RnZ_i^4 e^4 \ln \Lambda^{i/i}}{4\pi e_0^2 m_i^2 v_{th}} \approx 1.18 \times 10^{-3} \frac{Rn^{19} Z_{eff}}{T_k^2}, \quad (1)$$

where R is the major radius in meters, n the density, Z_i the nuclear charge number, e the elementary charge, $\ln \Lambda^{i/i}$ the coulomb logarithm, m_i the ion-mass, v_{th} the ion-thermal speed, n^{19} the density in units of 10^{19} m^{-3} , Z_{eff} the effective nuclear charge number and T_k the ion temperature in units of keV. The collision frequency in the equation shown earlier is normalized to v_{th}/R , where $v_{th} = \sqrt{2T/m_i}$ is the thermal velocity. To give a relation to experiments, some values have been calculated for typical cases: ITER-prediction¹⁷ ($R_{ref} = 6$, $n_{ref}^{19} = 12$, $Z_{eff} = 1.9$, $T_{ref} = 15$): $\nu_{ii} = 6 \times 10^{-4}$, simulated ITER discharge in DIII-D, shot 81499, cyclone base case^{3,18} ($R_{ref} = 1.7$, $n_{ref}^{19} = 5$, $Z_{eff} = 1.9$, $T_{ref} = 3$): $\nu_{ii} = 2 \times 10^{-3}$, DIII-D shot 128913, shortfall-case at edge^{19,20} ($R_{ref} = 1.7$, $n_{ref}^{19} = 1.2$, $Z_{eff} = 1.3$, $T_{ref} = 0.27$): $\nu_{ii} = 4 \times 10^{-2}$.

A sample result, a simulation with $\nu_{ii} = 1.2 \times 10^{-3}$, is shown in Fig. 1. The already described behaviour of the zonal potential ϕ (blue line in the online version) can be seen: an initial charge perturbation leads to a decaying GAM-oscillation revealing a zonal flow potential that is slowly damped by collisions. As the time in which the evolution of the potential can be observed is limited, the following method is used to obtain the evolution of the collisionally damped residual potential for early times, where the oscillation of the GAM is present: The mean value of the two neighbouring maxima of the GAM-oscillation is used together with the value of the intermediate minimum (cyan + in Fig. 1) to estimate the value of the potential (red x in Fig. 1) at the time of the minimum. A similar calculation is made using two minima and one maximum to estimate the potential at the time of the corresponding maximum. Using all possible values, a good approximation of the potential is obtained, which is depicted (dashed red curve) in Fig. 1. This approximation is valid if the change in the GAM’s oscillation and in its decay is sufficiently small, which is already given very early in the simulation. For very late times, when the GAM has been strongly damped, a time average of the potential evolution over the GAM’s oscillation’s period is taken to ensure compliance with the data from early times.

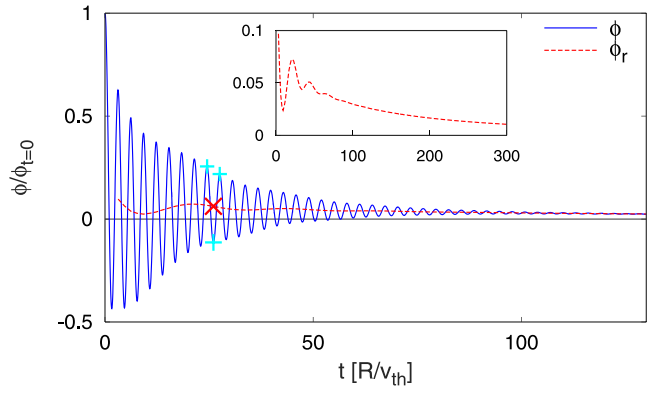


FIG. 1. Time evolution of the electrostatic potential ϕ (blue in the online version) and the collisionally damped residual potential, where the influence of the GAM is removed (dashed red line in the online version), for a simulation with $q = 1.3$, $\varepsilon = 0.15$ and a collision frequency of $\nu_{ii} = 1.2 \times 10^{-3}$. To provide an example for the method to remove the GAM-influence several points are marked: To calculate one point of the potential (red x in the online version), two maxima and one minima are marked (cyan + in the online version). The small box shows the long time decay of the potential.

Following this procedure, an analysis of the collisional damping of the zonal flow is undertaken varying the collision frequency ν_{ii} between 10^{-5} and 10^{-1} . The influence of the inverse aspect ratio and the safety factor are also studied, varying ε at $q = \{1.3, 1.4\}$. The time evolution of the potential can be roughly described with an exponential decay, i.e., $\phi(t) = \phi_a \exp[-\nu_D t]$, and a zonal flow damping rate (ν_D) can be determined. This damping rate is shown in Fig. 2 as a function of the collision frequency, showing a nearly linear relation $\nu_D \approx \alpha \nu_{ii}$.

The agreement between the analytic model and the numerical simulations is good at sufficiently low collision frequencies, and less satisfactory at higher collision frequencies. The predicted influence of ε and q (not shown) on the collisionless residual can be reproduced numerically (see also Ref. 13). Furthermore, for high collision frequencies the damped residual zonal flow converges to a finite stationary value within the simulated time interval. The latter undamped zonal flow corresponds to a purely toroidally rotating plasma, with the numerically obtained result in good agreement with the prediction of Ref. 14.

III. ANALYSIS OF THE FINITE HEAT FLUX THRESHOLD

To examine the influence of collisions on the heat flux and the finite heat flux threshold, a set of nonlinear flux-tube simulations is carried out with GKW. For this task, the parameters are chosen to be compliant to the well known cyclone base case: safety factor $q = 1.4$, magnetic shear $\hat{s} = 0.78$, inverse aspect ratio $\varepsilon = 0.19$, density gradient $R/L_n = 2.2$, and electron to ion temperature ratio $T_e/T_i = 1$. The geometry, however, is not modelled by the $\hat{s} - \alpha$ geometry as in Ref. 3, but rather with the use of a circular flux surface geometry that keeps all orders in the inverse aspect ratio. This choice leads to a change in the Dimits shift (from 6.0 for $\hat{s} - \alpha$ to 4.7 for the circular geometry) and also influences the finite heat flux threshold.⁶ The grid is chosen as follows: the number of radial modes $N_x = 83$, the number of toroidal modes $N_y = 21$, the number of grid points along the field line $N_s = 16$, the number of magnetic moment grid points $N_\mu = 9$, and the number of parallel velocity grid points $N_{v_\parallel} = 64$. For the zonal mode, the sixth order scheme along the magnetic field is used, and the dissipation

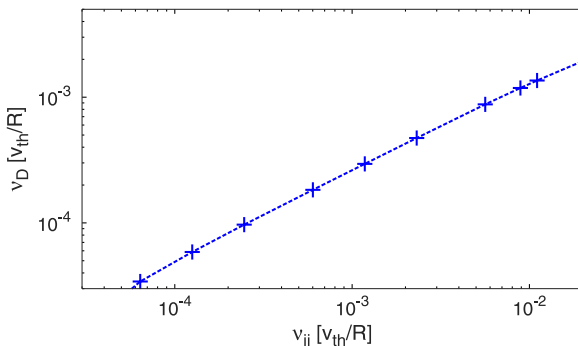


FIG. 2. Zonal flow damping rate as a function of the collision frequency. Simulations are indicated with the “+” symbol, while the line represents the analytic result of Ref. 14.

coefficients are $D_x = 0.1$, $D_y = 0.1$, $D_s = 1$, and $D_{v_\parallel} = 0.1$. A detailed description of the implementation and its effect on the dissipation can be found in Ref. 6. Following this analysis, the exponential damping rate due to the chosen grid is expected to be $|\gamma_d^{(6)}| = 1.9 \times 10^{-4}$ normalized to v_{th}/R and might only have an influence on the simulations with lower collision frequencies. A comparison of the zonal flow damping due to this resolution with the one due to the resolution used in Sec. II shows no significant differences in the damping. The temperature gradient is varied in a range of $R/L_T \in [3.0, 16.0]$, where the main part of the simulations is focused on the area around the finite heat flux threshold. Ion-ion collisions are, similar to the earlier study, treated with pitch-angle scattering, varying the collision frequency in a range of $\nu_{ii} \in [10^{-5}, 1]$.

Previous studies of collisionless ITG turbulence have shown that there are three specific ion temperature gradients lengths in the zonal-flow/ITG system that are relevant to the description of the heat flux near the threshold: the gradient length of linear stability $R/L_{T,lin}$, the Dimits gradient length $R/L_{T,Dim}$,³ and the finite heat flux threshold $R/L_{T,fh}$,^{5,6} with $R/L_{T,lin} < R/L_{T,Dim} < R/L_{T,fh}$. Here, the Dimits threshold is defined as the gradient length for which the extrapolated heat flux goes through zero, with the heat fluxes used in the extrapolation being obtained for gradient lengths well above the threshold. The finite heat flux threshold is the temperature gradient length below which a vanishing heat flux is found, i.e., it is the temperature gradient length at which the heat flux is discontinuous. In light of the findings outlined above, it is natural to divide the gradient length parameter space into three zones: I $R/L_{T,lin} < R/L_T < R/L_{T,Dim}$, II $R/L_{T,Dim} < R/L_T < R/L_{T,fh}$, and III $R/L_T > R/L_{T,fh}$ (see Fig. 3). Indeed, it will be shown later that the influence of collisions on the heat flux is very different in these three regions.

In general, the observed time evolution of the flux surface averaged heat flux can be described as follows (some examples are presented in Fig. 4, the corresponding shearing rate is shown in Fig. 5 and will be discussed later on): After a short initial “linear” growth due to the ITG-instability, a turbulent state with a finite heat flux develops. If the temperature gradient length is far below the finite heat flux threshold (i.e., in region I and to some extent in region II close to the border with region I), the turbulent state hardly develops.

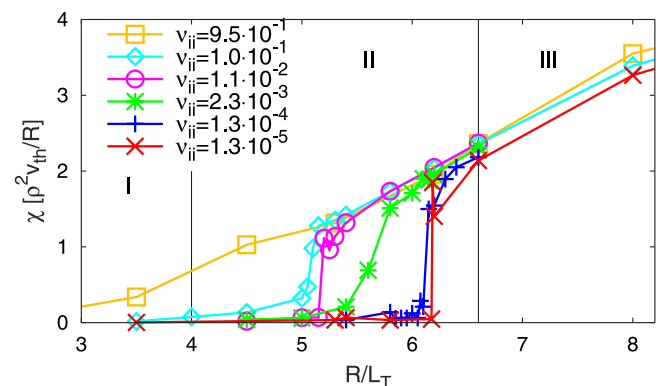


FIG. 3. Heat conduction coefficient χ depending on R/L_T for different ν_{ii} .

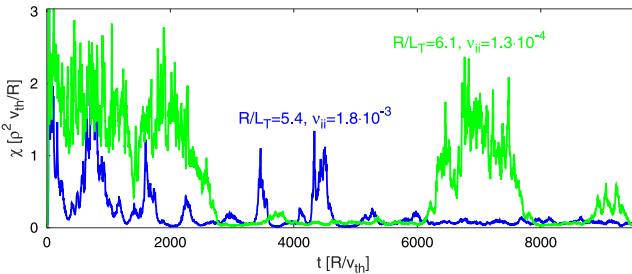


FIG. 4. Time evolution of the heat conductivity χ of simulations at $R/L_T = 5.4$ with $\nu_{ii} = 1.8 \times 10^{-3}$ (colour online blue), and at $R/L_T = 6.1$ with $\nu_{ii} = 1.3 \times 10^{-4}$ (colour online green). These simulations are located in zone II and are close to the finite heat flux threshold.

The zonal flows quickly suppress the turbulence, and a state of vanishing heat flux results. This is the physics picture described in Ref. 3. Closer to the finite heat flux threshold (region II), the turbulent state can persist for a long time before the turbulence is eventually suppressed. Additionally, a temporary inversion of states, from a high to a low heat flux state and vice versa, can be observed. Thus, for the evaluation of the heat flux and the heat conductivity, care has to be taken that the simulation has reached a proper stationary state. For gradient lengths above the finite heat flux threshold (region III), the turbulence remains in a high heat flux state for the entire duration of the simulation.

It should be noted that only two states are properly discernible. Below the finite heat flux threshold, a state where the turbulence is suppressed, and the heat flux is close to zero, is found. Only a small baseline turbulence that drives the zonal flow against the collisional dissipation remains. Above, a state where turbulence is only partially suppressed, and the heat flux is finite (heat conduction $\chi \gtrsim 1$) due to mediation by avalanches, is present. The physics picture that even in the low heat flux state the zonal flow can be driven against the collisional dissipation is confirmed by a study of the free energy transfer. For the low heat flux state with a collision frequency $\nu_{ii} = 1.3 \times 10^{-4}$, the free energy source due to the heat flux in the ion temperature gradient ($Q_i R / L_t$) is well in excess of the free energy transferred to the zonal

flow through the nonlinear interaction. The latter energy transfer, in turn is larger than the collisional dissipation. Nevertheless, an in-depth analysis, as carried out in Ref. 21 appears as a rewarding topic for future investigations.

If the parameters close to the finite heat flux threshold are chosen, the fragile states with a transposition of the two states are found. This transposition appears below and above the finite heat flux threshold and was already observed in Ref. 6. Slightly below the threshold, these simulations show flares where a finite heat flux appears for a reasonable time interval ($\gtrsim 1000R/v_{th}$). Slightly above the threshold, short periods with a suppressed heat flux are found, but the transposed state appears less pronounced as below the threshold. Generally, this transposition is found to appear at lower collision frequencies.

Two examples of simulations with such a transposition below the finite heat flux threshold are presented in Fig. 4, where the time evolution of the heat conductivities for the two simulations at $R/L_T = 5.4$, $\nu_{ii} = 1.8 \times 10^{-3}$ and at $R/L_T = 6.1$, $\nu_{ii} = 1.3 \times 10^{-4}$ are shown. The latter simulation nicely shows the transposition: the turbulence is suppressed at $t \approx 3000$ (time is normalized to R/v_{th}) and the simulation remains in the suppressed state for 3000 time units before a flare in $t \in [6000, 8000]$ appears, afterwards the simulation remains in the suppressed state until the end of the simulation (a period of 6000, not depicted in Fig. 4). In the evolution of the heat conductivity of the simulation at $\nu_{ii} = 1.8 \times 10^{-3}$ this behaviour, albeit less pronounced, can also be seen: a relatively quiet time in $t \in [1800, 3400]$ is followed up by two flares at $t \approx 3400$ and $t \approx 4200$.

Furthermore, these simulations can be used to demonstrate the influence of the avalanches. Therefore, the time evolution of the radial profile of the heat conductivity is presented in Fig. 6.

The structure and radial propagation of the avalanches is visible, for example, in the inset depicting the time period $t \in [6600, 6900]$ (note the periodic boundary conditions). Similar to the results of Ref. 6, the corresponding structures are also found in the perturbed temperature gradient. As previously observed, the perturbed temperature gradient,

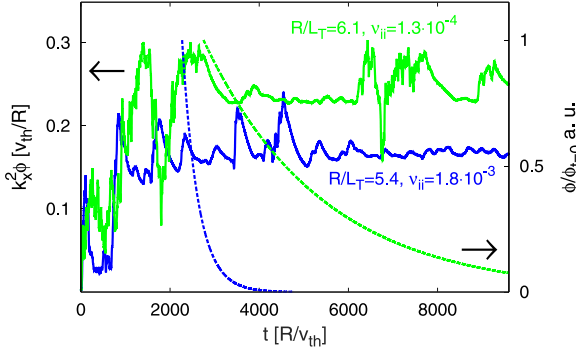


FIG. 5. Time evolution of the shearing rate $k_x^2 \phi$ for simulations at $R/L_T = 5.4$, $\nu_{ii} = 1.8 \times 10^{-3}$ and at $R/L_T = 6.1$, $\nu_{ii} = 1.3 \times 10^{-4}$ (both zone II), represented on the left y-axis. To give an idea for the estimated decay of the zonal flow potential, the results from the linear analysis in Sec. II are added at the corresponding times, being represented on the right y-axis. Data from simulations with collision frequencies of $\nu_{ii} = 1.3 \times 10^{-4}$ and $\nu_{ii} = 2.3 \times 10^{-3}$ are used, respectively. The data were adapted to the parameters used in this analysis according to the model of Ref. 14.

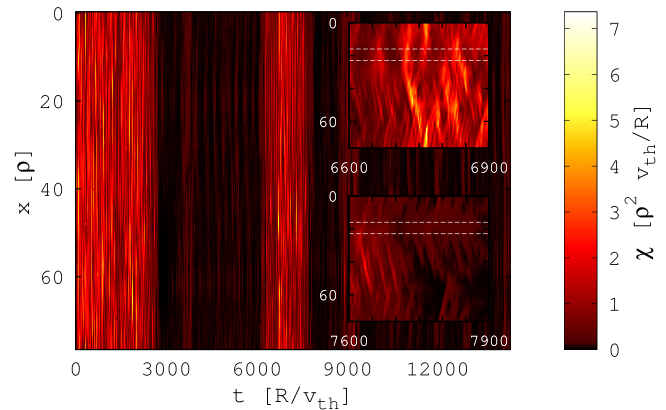


FIG. 6. Time evolution of the radial profile of the heat conductivity χ for a simulation at $R/L_T = 6.1$ and $\nu_{ii} = 1.3 \times 10^{-4}$. The insets show a short turbulent time period (top) and a period at the transition to the suppressed state (bottom). The area where avalanches emerge is marked with dashed white lines and is located radially at approximately $20R$.

averaged over the turbulent period, shows a decrease in the area where the avalanches are generated and also a decrease where the avalanches disappear (these areas correspond with the flanks of the staircases, as discussed in detail later). A clear correlation of the avalanche activity with the time evolution of the averaged heat conductivity in Fig. 4 can be seen. The correlation between the avalanches and a finite heat flux is paradigmatic not only for the transposing simulations, but for all simulations. For gradient lengths just above the finite heat flux threshold as well as for the transposing states, the avalanches are identified as the main reason for a finite heat flux. Further examinations of these simulations follow in Secs. IV and V.

Figure 3 shows the heat conduction coefficient χ as a function of the gradient length for different values of the collision frequency. The heat conduction coefficients in this figure have been averaged over sufficient long time intervals to address the possible intermittent behaviour of the heat flux. For vanishing ν_{ii} the results of a collisionless study⁶ are reproduced, with only slight differences, which are connected with the different resolution used in this paper. It can be directly observed that the susceptibility towards collisional effects is very different in the three regions. In region I and III, i.e., below the Dimits gradient length or above the finite heat flux threshold, the collision frequencies $\nu_{ii} > 0.1$ are required to generate a still relatively small change in the heat flux. To put this in perspective, at $R = 1.7\text{ m}$, $n = 4 \times 10^{19}\text{ m}^{-3}$, this corresponds to a temperature $T \approx 250\text{ eV}$. Therefore, the collisional damping of the zonal flows above the finite heat flux threshold or below the Dimits threshold is, in the present day experiments, important only in the outer edge of L-mode discharges. The influence of collisions is, however, much larger in the region II. Already at moderate collision frequencies, the finite heat flux threshold gradient length ($R/L_{T,\text{f}}$) is reduced with the increasing ν_{ii} . A clear step in the heat flux, with no clear sign of a flattening of the heat conduction versus the temperature gradient length curve, however, remains visible up to high collision frequencies ($\nu_{ii} > 0.1$). Only at very high values of the collision frequency ($\nu_{ii} \approx 1$) does the heat flux go smoothly to zero.

A steep threshold is also observed in the heat conduction coefficient (χ) as a function of collision frequency as shown in Fig. 7. As stated before, the heat conduction coefficient

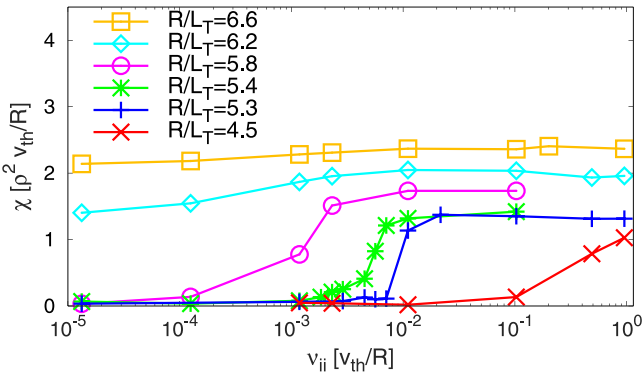


FIG. 7. Heat conduction coefficient χ depending on ν_{ii} for different R/L_T chosen from region II.

obtained in the region I and III ($R/L_T = 4.5, 6.2$, and 6.4) only changes at high collision frequencies. For R/L_T in region II, χ shows a threshold, which changes its position towards lower ν_{ii} and considerably softens for increasing R/L_T . Here also a slight increase of the heat flux below the finite heat flux threshold can be observed, which manifests both in the mean value of the baseline turbulence and also in an increased appearance and markedness of small unsuppressed turbulence flares in the (not shown) time traces. Above the finite heat flux threshold, the influence of the collisions becomes less pronounced.

Figure 8 shows the finite heat flux threshold as a function of ν_{ii} . Here, the threshold for each ν_{ii} is determined as the lowest value of R/L_T where χ has a (proper) finite value. For $\nu_{ii} = 9.5 \times 10^{-1}$, the threshold is set to the value where the heat flux vanishes ($R/L_T = 3.5$). It follows that the difference between the finite heat flux threshold and the Dimits threshold is significant up to relatively high collision frequencies. In collisionless simulations, it was found that it can take a considerable time for the heat flux to settle in the low heat flux state, especially close to the finite heat flux threshold.⁶ Indeed, close to this threshold a very small collision frequency is sufficient to generate a finite heat flux. However, further below the collisionless finite heat flux threshold, the system settles in a considerable shorter time, and a higher collision frequency is required to generate a high heat flux. In modern day experiments and certainly in ITER, the heat flux is predicted to have a discontinuous behaviour as a function of R/L_T . However, it should be noted that, as seen if the temperature gradient is considered a function of the heat flux, this behaviour should be contemplated cautiously as an exact analysis and the flux driven simulations might be employed. Nevertheless, the gradient driven simulations provide important conclusions on the collisional behaviour.

The analysis of the dependence of the heat flux on the collision frequency allows a comparison with the work presented in Ref. 4. In the latter reference a rise of the heat flux with the increasing collision frequency was found. The results presented here suggest a somewhat steeper, discontinuous transition, from a state with vanishing heat flux to a

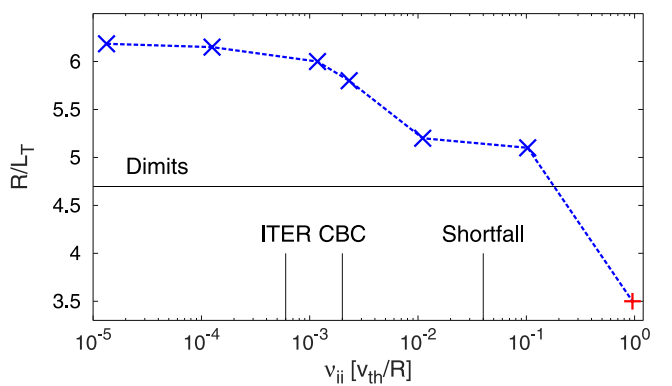


FIG. 8. Position of the finite heat flux threshold as a function of the collision frequency marked as x (blue in the online version). The estimated threshold for very high ν_{ii} is added as + (red in the online version). The position of the three sample collision frequencies given in Sec. II is depicted. Also the value of the Dimits threshold $R/L_{T,\text{Dim}} = 4.7$ is indicated.

state with a finite heat flux. Although the rise in the heat flux with the collision frequency is qualitatively similar, it should be noted that the interpretation of the turbulent state is rather different. In Ref. 4 it is assumed that the value $R/L_T = 5.3$ lies below the Dimits threshold, whereas in this paper this value is shown to lie above the Dimits threshold but below the finite heat flux threshold. It is furthermore noted that much larger time intervals have been used in this paper. It has been found that these long time intervals are essential to obtain the correct heat flux at values close to the threshold.

IV. ANALYSIS OF THE SHEAR INTENSITY

The finite heat flux threshold is connected with a radial structure formation known as staircase. Before investigating the radial profiles of the shearing rate, in this section, the magnitude of the shearing rate as a function of the parameters is investigated. The focus is on the shearing rate ($\omega_{E \times B}$) of the lowest radial wave vector in the computational domain since it is the wavelength of this mode that sets the radial scale length of the staircase close to the finite heat flux threshold.

Figure 9 shows the values of this shearing rate $\omega_{E \times B} = k_x^2 \phi / R$, normalized with v_{th}/R , as a function of the gradient length R/L_T for the simulations of Figs. 3 and 7. The shearing rate as a function of R/L_T shows a similar behaviour for all values of the collision frequency. The shearing rate is small for values of the temperature gradient length well below the finite heat flux threshold and increases almost linearly with R/L_T , having the same value for all the collision frequencies. At the corresponding collisional finite heat flux threshold, a change in the slope of the shearing rate as a function of the gradient length is observed, with the shearing rate decreasing when further increasing the gradient length. In accordance with the behaviour of the finite heat flux threshold, the gradient length of this change is reduced if the collision frequency is raised. As a consequence of this behaviour, a lower maximum shearing rate is found for higher collision frequencies. It is noted, that a small parameter region in R/L_T exists, where a relatively high value of the shearing rate is paired with a finite heat flux. This shows that the absolute value of the long wave length zonal mode amplitude is not the only factor that determines the turbulence suppression. The simultaneous occurrence of a high heat flux and a high ExB shear is

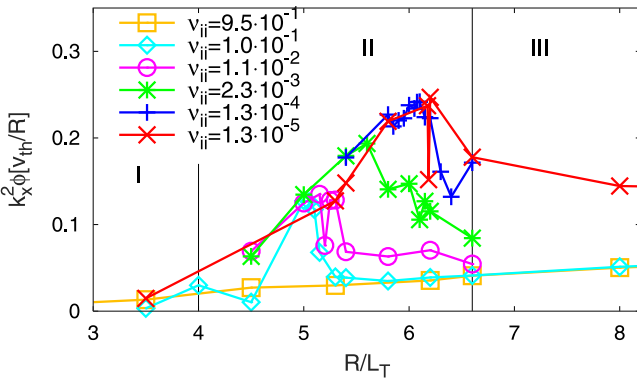


FIG. 9. Zonal flow shear strength of the zero mode depending on R/L_T for various ν_{ii} .

relatively insensitive to the collision frequency, but the region in R/L_T where it occurs shifts downward with the increasing collision frequency, which signals that the proximity to the finite heat flux threshold is important.

Figure 10 shows the shearing rate as a function of collision frequency for various values of the temperature gradient length. For the intermediate R/L_T (below the collisionless threshold at $R/L_T = 6.2$), the shearing rate shows a slight increase when ν_{ii} is increased. At collision frequencies that correspond to the finite heat flux threshold, the shearing rate drops quickly and finally slowly decays towards a finite value for high collision frequency. The latter value appears to be almost independent of the gradient length. At high R/L_T , above the collisionless threshold, the shearing rate decays more smoothly towards the same finite value for high ν_{ii} . It is noted that the latter simulations show a smaller shearing rate when compared with the shearing rate that is obtained at the finite heat flux thresholds in simulations with smaller temperature gradient lengths.

We interpret the results shown earlier as follows: Below the finite heat flux threshold (but above the Dimits threshold) the turbulence drives the long wave length zonal flow mode connected with the staircase formation until it is large enough to suppress the turbulence. Since the growth rate (γ) of the ITG depends on the gradient length, but is, at these values of the collision frequency, relatively insensitive to the collision frequency, the shear values required for turbulence stabilization ($\omega_{E \times B} \approx \gamma$) scales roughly linear with the gradient length. For this reason, the shearing rate is observed to increase with R/L_T independent of the collision frequency. Above the finite heat flux threshold, the shearing rate is observed to decay with increasing R/L_T , despite the increase in turbulence intensity and heat flux. This result is quite contrary to the usual discussion on zonal flow development, where the zonal flow is driven by the modulation instability and saturates over collisional damping or nonlinear terms connected with the zonal flow amplitude. In the latter scenario, one would not predict a reduction in the zonal mode amplitude with increasing R/L_T at constant collision frequency. Here, it appears that the increase in turbulence intensity leads to a reduction in the zonal flow. The reason for this is at present unknown. Either the turbulence directly acts to decrease the zonal flow amplitude, or the turbulence drives the zonal

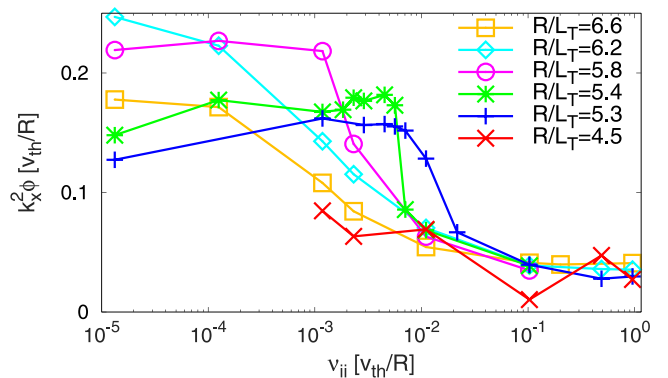


FIG. 10. Zonal flow shear strength of the zero mode depending on ν_{ii} for various R/L_T .

flow less effectively. There does not appear to be a satisfactory physics picture for either of these explanations. It should also be noted, however, that the results shown in Fig. 10 concern the long wave length zonal flow only, and do not reflect on the shorter wavelength shear layers. The physics governing the different length scales of the zonal flow are possibly very different. The reduction in the finite heat flux threshold with the collision frequency can be explained as follows: In collisionless simulations, it is observed that the time the system takes to settle in the low heat flux state increases as the finite heat flux threshold is approached. The long wave length zonal flows take longer to develop as the gradient length is increased and, therefore, collisions affect the heat flux most strongly at gradient lengths closer to the threshold.

The evidence for the influence of staircases can be seen in an examination of the shearing rate of the simulations showing a transposition of states mentioned in Sec. III. In Fig. 5 (in Sec. III), the time evolution of the shear intensities for simulations at $R/L_T = 5.4$, $\nu_{ii} = 1.8 \times 10^{-3}$ and at $R/L_T = 6.1$, $\nu_{ii} = 1.3 \times 10^{-4}$ are depicted next to their heat conduction coefficients shown in Fig. 4. There are several noteworthy observations. As commonly known, the initial turbulence leads to a growth of the shear intensity. Following the interpretation,^{1,4} a suppression of the turbulence with a subsequent collisional decay of the shear intensity and the emergence of an oscillatory behaviour should be observed. For the simulation at $R/L_T = 5.4$, $\nu_{ii} = 1.8 \times 10^{-3}$, this behaviour can be roughly made out for early times $t \leq 5000$, but not for later times. In the data of the simulation with a lower collision frequency at $R/L_T = 6.1$, $\nu_{ii} = 1.3 \times 10^{-4}$, this behaviour is hardly recognisable at all. Furthermore, for later times in all simulations below the finite heat flux threshold, the state with the vanishing heat flux is present and does not show an oscillating behaviour of the turbulence. The simulations showing the transposing behaviour are also in this state in between two flares, for example $t \in [3000, 6000]$ in Figs. 3 and 4 for $R/L_T = 6.1$, $\nu_{ii} = 1.3 \times 10^{-4}$ or less pronounced in the simulation with higher collision frequency in the period where $t \in [1800, 3400]$. Also, the time of simulation in this state is considerably longer than one would expect if the decay of the zonal flow potential is considered. To point this out, the expected decay of the zonal flow potential is depicted at the according position in Fig. 5. It is calculated with the results obtained in Sec. II for collision frequencies of $\nu_{ii} = 1.3 \times 10^{-4}$ and $\nu_{ii} = 2.3 \times 10^{-3}$ to match the frequencies respectively. The data is adapted to the parameters used in this analysis (described in Sec. III) according to the model of Ref. 14. Although the data was obtained with a much higher resolution, it is still relevant (see discussion in Sec. III). Here it can be seen, that the zonal potential from the linear analysis already would have been significantly decayed before another flare erupts. Although the intensity of the shear shows a decay resembling the one predicted by the linear analysis, it does so only for a very short time and then stays rather constant at a relatively high value due to a baseline turbulence before another flare appears. This shows that the potential does not follow the proposed decay. This becomes exceptionally clear, when not the period between two flares is considered, but the

period after the last flare: $t \geq 5000$ for the simulation with a higher collision frequency and $t \geq 8000$ for the simulation with lower collision frequency (here the simulation ran until $t = 14\,400$). In that time the zonal flow should have decayed, and turbulence reappeared, which is not the case.

V. ANALYSIS OF THE RADIAL SHEAR PROFILE

Further insight can be gained from the shape of the radial shear profile. Nearly all of the simulations described in this paper show so-called staircases in their radial shear profile, i.e., self-organized shear flow structures,^{7–9} which require long timescales to develop properly. They have been classified⁶ into fully (box-shaped in gradient-driven simulations) and partially developed (sawtooth shaped in gradient-driven simulations) staircases. A fully developed staircase is thought to suppress turbulence as it allows a sufficiently high shear over nearly all of the radial domain. A partial developed staircase has a wider region with a low shearing rate (compared with the associated ITG growth rate) and allows heat flux avalanches to originate from such regions, leading to a finite heat flux. An example of these forms can be seen in Fig. 11: a fully developed staircase at $\nu_{ii} = 4.5 \times 10^{-3}$, a partially developed staircase at $\nu_{ii} = 1.1 \times 10^{-2}$. We assume that staircases form with specific radial extends and are not affected by the boundary conditions imposed in the radial direction due to the box-size test carried out in Ref. 5.

In the simulations carried out in this analysis, the expected correlation with the finite heat flux threshold is found not only, as already previously examined, in the direction of the temperature gradient length, but also if the finite heat flux threshold is passed in the collision frequency. As an example for this, Fig. 11 presents the radial shear profiles averaged over a substantial time period of simulations with different collision frequencies for a fixed temperature gradient length of $R/L_T = 5.3$. For the chosen temperature gradient length, the finite heat flux threshold (in ν_{ii} -direction) is located at $\nu_{ii} = 1.1 \times 10^{-2}$ following the definition given in Sec. III. Below the finite heat flux threshold, the fully developed staircases are present at times when turbulence is suppressed, for example the shear profile at $\nu_{ii} = 4.5 \times 10^{-3}$ in

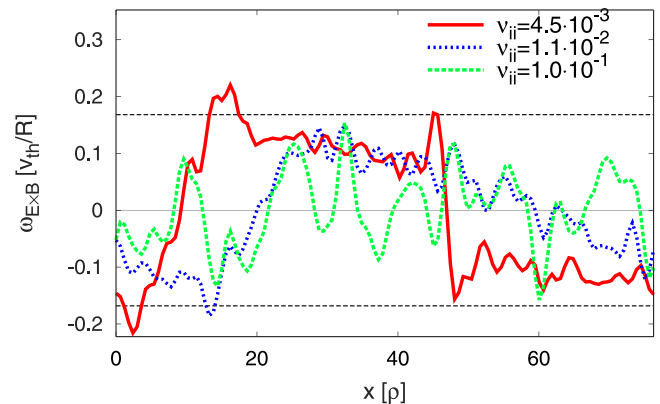


FIG. 11. Radial shear profile for different ν_{ii} at a fixed temperature gradient length of $R/L_T = 5.3$. The dashed black line represents the corresponding growth rate for the most unstable ITG-mode.

Fig. 11. Slightly above the threshold, the partially developed staircases are present, as visible in the shear profile at $\nu_{ii} = 1.1 \times 10^{-2}$ in Fig. 11. Here, the avalanches emerge from the region where the shear is low $\omega_{E \times B} \ll \gamma$ and propagate through the regions where the shear is high $\omega_{E \times B} \approx \gamma$, which leads to a finite heat flux. It should be noted, that in all simulations with a partial staircase, it was observed that the softening of the flank occurred at the transition where the shear changes its value from approximately $+\gamma$ to $-\gamma$. At very high collision frequencies, no discernible structures are found, a paradigmatic radial profile is shown for $\nu_{ii} = 1.0 \times 10^{-1}$. Furthermore, it should be noted that the simulations above the finite heat flux threshold show significantly higher fluctuations in the radial shear profile. This is thought to be a consequence of the turbulent activity.

As already pointed out in Ref. 6, the change of the staircase type can also be seen in the different time periods of the simulations, which show a transposition of states. To exemplify this, the radial shear profile of the simulation at $R/L_T = 6.1$, $\nu_{ii} = 1.3 \times 10^{-4}$, averaged in time periods representing the different states, is shown in Fig. 12. If the profiles of the different times are related to the time evolution of the heat conduction coefficient presented in Fig. 4, the correspondence between times, where a fully developed staircase is present and periods where the heat flux is suppressed, and vice versa, is clearly visible. In the periods $t \in [3000, 6000]$ and $t \in [8000, 14400]$, where the heat flux is suppressed, the radial shear profile shows a fully developed (box-shaped) staircase structure. Whereas in the time range $t \in [6000, 8000]$, a finite heat flux is present, and the radial shear profile shows the structure of a partial staircase. This can also be seen in the avalanche activity visible in the radial profile of the heat conduction coefficient presented in Fig. 6. Here, it can also be nicely seen that the avalanches emerge from the softened flank of the staircase. The softened flank of the staircase for $t \in [6000, 8000]$ lies at approximately 20ρ and leads to an area of low shear around it, as visible in Fig. 12. This area corresponds to the area where the avalanches emerge, indicated with the dashed white lines in Fig. 6.

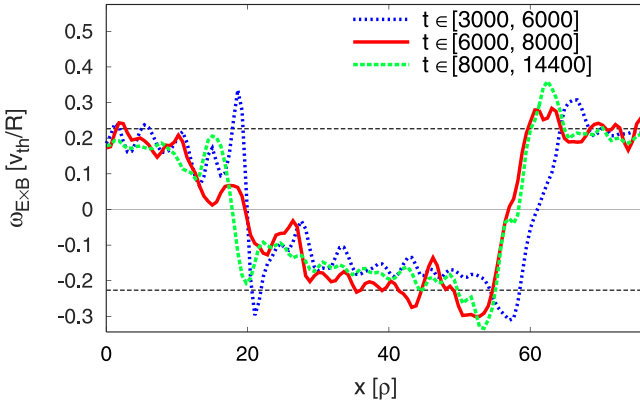


FIG. 12. Radial shear profile of the simulation at $R/L_T = 6.1$, $\nu_{ii} = 1.3 \times 10^{-4}$. The shear is averaged in different times representing the different states, visible for example in the heat conduction coefficient depicted in Fig. 3. The dashed black line represents the corresponding growth rate for the most unstable ITG-mode.

We interpret the results as follows: The form of staircase stands in direct correlation to the heat flux. A fully developed staircase allows a high shear, meaning about the same magnitude as the growth rate of the fastest growing corresponding ITG mode, over nearly the whole radial domain. This effectively suppresses turbulence. Also, for this form, the regions where the shear is low are considerably small and thus, the heat flux avalanches cannot emerge from these regions. If the structure changes to a partial staircase i.e., the flank softens, the region where the shear is low is wide enough to allow heat flux avalanches to be generated. They propagate through the regions where the shear is high and thus lead to a finite heat flux over nearly the whole radial domain. As the transition appears both if R/L_T or the collision frequency is increased, the mechanism causing this structure appears to be susceptible to both effects. Furthermore, the transposition of states over a significant time shows that the staircase structure, albeit small, has stability. Very high collision frequencies do not allow the formation of not even a partial staircase. This is thought to explain the second shift at high collision frequencies in the threshold seen in Fig. 8 and the corresponding linear behaviour.

VI. CONCLUSION

In this work, the influence of collisions on the ion temperature gradient driven heat flux, close to the nonlinear threshold has been examined. The impact of collisions, in particular, on the finite heat flux threshold is investigated, and the following results have been obtained.

The decay of the zonal potential has been examined in the Rosenbluth-Hinton test, and is compared with the analytical model of Ref. 14. The numerically obtained zonal flow collisional decay rates agree well with the analytic prediction for low collision frequencies, while higher frequencies yielded somewhat less satisfactory results. Furthermore, the influence of the safety factor and the inverse aspect ratio, and the remaining residual zonal flow not affected by collisions have been reproduced.

The behaviour of the finite heat flux threshold has been examined by an extensive scan in the temperature gradient length and the collision frequency. In the simulations generally two distinct states are visible: a state where the turbulence is suppressed, and the heat flux almost vanishes, and a state with a finite heat flux. For some parameters, a transposition of both states for a considerable time period is observed. Three different temperature gradient lengths that characterize the near threshold dynamics have been identified: the gradient length of linear stability $R/L_{T,\text{lin}}$, the Dimits gradient length $R/L_{T,\text{Dim}}$, and the finite heat flux threshold $R/L_{T,\text{fh}}$, where $R/L_{T,\text{lin}} < R/L_{T,\text{Dim}} < R/L_{T,\text{fh}}$ applies. It is found, that the influence of the collisions is most prominent in the region where $R/L_{T,\text{Dim}} < R/L_T < R/L_{T,\text{fh}}$. Here, only small changes in the collision frequency lead to a noticeable shift of the finite heat flux threshold towards the lower R/L_T , while outside of this region the influence of collisions is minimal and very high collision frequencies are required to produce a significant change of the heat flux. A comparison of the time spent in the vanishing heat flux state and the

collisional zonal flow decay time, reveals that the potential would have decayed substantially long before the end of the state is reached. For sufficient small collision frequencies, the zonal flow can, therefore, be driven against the collisional dissipation even when the heat flux is vanishingly small. Despite the reduction of the finite heat flux threshold with the increasing collision frequency, it remains considerably larger compared with the interpolated Dimits threshold for collision frequencies relevant to current experiments.

For a fixed collision frequency, the shear rate of the longest wave length radial mode increases almost linearly with R/L_T up to the value of the finite heat flux threshold; for larger values a decay is observed. Only very high collision frequencies lead to a suppression of this behaviour. The latter decay suggests that a saturation mechanism of the zonal flow is directly related to the turbulence intensity. If the collision frequency is increased for a fixed R/L_T , the shear intensity stays relatively constant until the finite heat flux threshold is reached, then decays to a finite value for high collision frequencies. A small region, in the temperature gradient lengths, above the finite heat flux threshold is found, where a high shear intensity is paired with a finite heat flux, indicating that the contemplation of only the shear intensity is not sufficient for an explanation of the finite heat flux threshold.

The radial profile of the $\mathbf{E} \times \mathbf{B}$ shearing rate shows the staircase formation. The fully developed staircases (i.e., box shaped shearing rates) are observed below the finite heat flux threshold and lead to a suppression of turbulence with a vanishing heat flux. The partially developed staircases (which have the shapes of sawtooth) allow the appearance of avalanches and lead to a finite heat flux. The latter are observed above the finite heat flux threshold, both in the direction of R/L_T and the collision frequency. It was also observed that although the transition from a fully developed to a partially developed staircase requires only small changes in the collision frequency at the corresponding R/L_T , very high collision frequencies were required to suppress the formation of partial staircases themselves. The examination of staircases provided a satisfying explanation for the behaviour of the finite heat flux threshold. Nevertheless, a model to explain the influence of collisions on the formation and behaviour of the staircases remains to be desired.

¹P. H. Diamond, S.-I. Itoh, K. Itoh, and T. S. Hahm, “Zonal flows in plasma—A review,” *Plasma Phys. Controlled Fusion* **47**(5), R35 (2005).

²H. Biglari, P. H. Diamond, and P. W. Terry, “Influence of sheared poloidal rotation on edge turbulence,” *Phys. Fluids B: Plasma Phys.* **2**(1), 1–4 (1990).

³A. M. Dimits, G. Bateman, M. A. Beer, B. I. Cohen, W. Dorland, G. W. Hammett, C. Kim, J. E. Kinsey, M. Kotschenreuther, A. H. Kritz, L. L. Lao, J. Mandrekas, W. M. Nevins, S. E. Parker, A. J. Redd, D. E.

Shumaker, R. Sydora, and J. Weiland, “Comparisons and physics basis of tokamak transport models and turbulence simulations,” *Phys. Plasmas* **7**(3), 969–983 (2000).

⁴Z. Lin, T. S. Hahm, W. W. Lee, W. M. Tang, and P. H. Diamond, “Effects of collisional zonal flow damping on turbulent transport,” *Phys. Rev. Lett.* **83**, 3645–3648 (1999).

⁵F. Rath, A. G. Peeters, R. Buchholz, S. R. Grosshauser, P. Migliano, A. Weikl, and D. Sintzhi, “Comparison of gradient and flux driven gyrokinetic turbulent transport,” *Phys. Plasmas* **23**(5), 052309 (2016).

⁶A. G. Peeters, F. Rath, R. Buchholz, Y. Camenen, J. Candy, F. J. Casson, S. R. Grosshauser, W. A. Hornsby, D. Sintzhi, and A. Weikl, “Gradient-driven flux-tube simulations of ion temperature gradient turbulence close to the non-linear threshold,” *Phys. Plasmas* **23**(8), 082517 (2016).

⁷G. Dif-Pradalier, V. Grandgirard, Y. Sarazin, X. Garbet, and P. Ghendrih, “Interplay between gyrokinetic turbulence, flows, and collisions: Perspectives on transport and poloidal rotation,” *Phys. Rev. Lett.* **103**, 065002 (2009).

⁸G. Dif-Pradalier, P. H. Diamond, V. Grandgirard, Y. Sarazin, J. Abiteboul, X. Garbet, P. Ghendrih, A. Strugarek, S. Ku, and C. S. Chang, “On the validity of the local diffusive paradigm in turbulent plasma transport,” *Phys. Rev. E* **82**, 025401 (2010).

⁹G. Dif-Pradalier, G. Hornung, P. Ghendrih, Y. Sarazin, F. Clairet, L. Vermare, P. H. Diamond, J. Abiteboul, T. Cartier-Michaud, C. Ehrlacher, D. Estève, X. Garbet, V. Grandgirard, O. D. Gürcan, P. Hennequin, Y. Kosuga, G. Latu, P. Maget, P. Morel, C. Norscini, R. Sabot, and A. Storelli, “Finding the elusive $\mathbf{E} \times \mathbf{B}$ staircase in magnetized plasmas,” *Phys. Rev. Lett.* **114**, 085004 (2015).

¹⁰X. Garbet and R. E. Waltz, “Heat flux driven ion turbulence,” *Phys. Plasmas* **5**(8), 2836–2845 (1998).

¹¹M. N. Rosenbluth and F. L. Hinton, “Poloidal flow driven by ion-temperature-gradient turbulence in tokamaks,” *Phys. Rev. Lett.* **80**, 724–727 (1998).

¹²X. Garbet, Y. Idomura, L. Villard, and T. Watanabe, “Gyrokinetic simulations of turbulent transport,” *Nucl. Fusion* **50**(4), 043002 (2010).

¹³A. Peeters, Y. Camenen, F. Casson, W. Hornsby, A. Snodin, D. Sintzhi, and G. Szepesi, “The nonlinear gyro-kinetic flux tube code GKW,” *Comput. Phys. Commun.* **180**(12), 2650–2672 (2009).

¹⁴Y. Xiao, P. J. Catto, and K. Molvig, “Collisional damping for ion temperature gradient mode driven zonal flow,” *Phys. Plasmas* **14**(3), 032302 (2007).

¹⁵X. Q. Xu, Z. Xiong, Z. Gao, W. M. Nevins, and G. R. McKee, “Tempest simulations of collisionless damping of geodesic-acoustic mode in edge plasma pedestal,” *Phys. Rev. Lett.* **100**, 215001 (May 2008).

¹⁶J. Candy and R. Waltz, “An eulerian gyrokinetic-maxwell solver,” *J. Comput. Phys.* **186**(2), 545–581 (2003).

¹⁷J. Candy, General Atomics Report No. GA-A28239, 2015.

¹⁸C. Greenfield, J. DeBoo, T. Osborne, F. Perkins, M. Rosenbluth, and D. Boucher, “Enhanced fusion performance due to plasma shape modification of simulated iter discharges in DIII-D,” *Nucl. Fusion* **37**(9), 1215 (1997).

¹⁹A. E. White, L. Schmitz, W. A. Peebles, T. A. Carter, T. L. Rhodes, E. J. Doyle, P. A. Gourdain, J. C. Hillesheim, G. Wang, C. Holland, G. R. Tynan, M. E. Austin, G. R. McKee, M. W. Shafer, K. H. Burrell, J. Candy, J. C. DeBoo, R. Prater, G. M. Staebler, R. E. Waltz, and M. A. Makowski, “A correlation electron cyclotron emission diagnostic and the importance of multifield fluctuation measurements for testing nonlinear gyrokinetic turbulence simulations,” *Rev. Sci. Instrum.* **79**(10), 103505 (2008).

²⁰C. Holland, A. E. White, G. R. McKee, M. W. Shafer, J. Candy, R. E. Waltz, L. Schmitz, and G. R. Tynan, “Implementation and application of two synthetic diagnostics for validating simulations of core tokamak turbulence,” *Phys. Plasmas* **16**(5), 052301 (2009).

²¹M. Nakata, T.-H. Watanabe, and H. Sugama, “Nonlinear entropy transfer via zonal flows in gyrokinetic plasma turbulence,” *Phys. Plasmas* **19**(2), 022303 (2012).